



Article

# Towards the Continuous Hydrothermal Synthesis of ZnO@Mg<sub>2</sub>Al-CO<sub>3</sub> Core-Shell Composite Nanomaterials

Ian Clark <sup>1,2</sup>, Jacob Smith <sup>1,2</sup>, Rachel L. Gomes <sup>2</sup> and Edward Lester <sup>1,\*</sup>

<sup>1</sup> Advanced Materials Research Group, Faculty of Engineering, University of Nottingham, University Park, Nottingham NG7 2RD, UK; ian.clark@nottingham.ac.uk (I.C.); jacob.smith@nottingham.ac.uk (J.S.)

<sup>2</sup> Food, Water, Waste Research Group, Faculty of Engineering, University of Nottingham, University Park, Nottingham NG7 2RD, UK; Rachel.gomes@nottingham.ac.uk

\* Correspondence: edward.lester@nottingham.ac.uk

Received: 17 September 2020; Accepted: 12 October 2020; Published: 16 October 2020



**Abstract:** Core-shell Zinc Oxide/Layered Double Hydroxide (ZnO@LDH) composite nanomaterials have been produced by a one-step continuous hydrothermal synthesis process, in an attempt to further enhance the application potential of layered double hydroxide (LDH) nanomaterials. The synthesis involves two hydrothermal reactors in series with the first producing a ZnO core and the second producing the Mg<sub>2</sub>Al-CO<sub>3</sub> shell. Crystal domain length of single phase ZnO and composite ZnO was 25 nm and 42 nm, respectively. The ZnO@LDH composite had a specific surface area of 76 m<sup>2</sup> g<sup>-1</sup>, which was larger than ZnO or Mg<sub>2</sub>Al-CO<sub>3</sub> when produced separately (53 m<sup>2</sup> g<sup>-1</sup> and 58 m<sup>2</sup> g<sup>-1</sup>, respectively). The increased specific surface area is attributed to the structural arrangement of the Mg<sub>2</sub>Al-CO<sub>3</sub> in the composite. Platelets are envisaged to nucleate on the core and grow outwards, thus reducing the face–face stacking that occurs in conventional Mg<sub>2</sub>Al-CO<sub>3</sub> synthesis. The Mg/Al ratio in the single phase LDH was close to the theoretical ratio of 2, but the Mg/Al ratio in the composite was 1.27 due to the formation of Zn<sub>2</sub>Al-CO<sub>3</sub> LDH from residual Zn<sup>2+</sup> ions. NaOH concentration was also found to influence Mg/Al ratio, with lower NaOH resulting in a lower Mg/Al ratio. NaOH concentration also affected morphology and specific surface area, with reduced NaOH content in the second reaction stage causing a dramatic increase in specific surface area (> 250 m<sup>2</sup> g<sup>-1</sup>). The formation of a core-shell composite material was achieved through continuous synthesis; however, the final product was not entirely ZnO@Mg<sub>2</sub>Al-CO<sub>3</sub>. The product contained a mixture of ZnO, Mg<sub>2</sub>Al-CO<sub>3</sub>, Zn<sub>2</sub>Al-CO<sub>3</sub>, and the composite material. Whilst further optimisation is required in order to remove other crystalline impurities from the synthesis, this research acts as a stepping stone towards the formation of composite materials via a one-step continuous synthesis.

**Keywords:** continuous hydrothermal synthesis; layered double hydroxide; composite; nano hybrid structures; Ultraviolet (UV) properties

## 1. Introduction

Layered double hydroxides (LDHs) are a type of anionic clay. LDHs conform to a general formula:  $[M_{1-x}^{II}M_x^{III}(\text{OH}_2)](A^{n-})_{x/n} \cdot z\text{H}_2\text{O}$  [1], where M<sup>II</sup> and M<sup>III</sup> represent bivalent (Mg<sup>2+</sup>, Ca<sup>2+</sup>, Co<sup>2+</sup>, Zn<sup>2+</sup>, Cu<sup>2+</sup>, Ni<sup>2+</sup>) and trivalent metal ions (Al<sup>3+</sup>, Co<sup>3+</sup>, Fe<sup>3+</sup>, Cr<sup>3+</sup>, Ni<sup>3+</sup>, Co<sup>3+</sup>) are distributed in brucite-like sheets [2]. A<sup>n-</sup> is representative of interlayer anions, which hold together the positively charged brucite-like sheets through electrostatic force. A figure detailing this structure can be found elsewhere [3]. Layered double hydroxides have been used as adsorbents for pollutant mitigation [4–7], drug delivery [8] flame-retarding polymers [9,10], catalysts [11,12], and as precursor materials for catalysts [13,14].

LDH core-shell materials could offer an interesting extension of current uses, since the LDH shell and core materials are joined without the need for binding agents. The core-shell composites could be tuned to have specific functionalities, such as photocatalysis combined with selective adsorption or drug release combined with magnetic properties. Magnetic core-shell LDHs have been used as drug delivery vehicles, produced via a two-step synthesis process whereby the magnetic ferrite core was produced in the first step, and then, the LDH shell was grown via a co-precipitation reaction step [15,16]. More recently, however, a variety of core nanoparticles have been incorporated into composites following the same two-stage synthesis protocol. Silica spheres surrounded by MgAl-CO<sub>3</sub> shells have been used to remove the anti-inflammatory drug diclofenac from wastewater [17,18]. Zeolites have also been employed as core materials for adsorbent composites for water treatment as a way to combine the high specific surface area of zeolites with the ion exchange functionality of LDHs [19,20]. It has been found that the micro-pore volume of the zeolite was reduced when the shell was synthesised in a zeolite@LDH composite [19]. To date, two stage hydrothermal synthesis reactions have been used primarily to produce nanowires on substrates [21–25]. Co<sub>3</sub>O<sub>4</sub> composites have been applied in electronics and the two-step batch hydrothermal method is preferred, as it provides materials as readymade electrodes [21,22]. ZnO@LDHs have also been utilised in photocatalytic applications along with TiO<sub>2</sub>@LDHs. TiO<sub>2</sub>@CoAl-CO<sub>3</sub> and ZnO@CuAl-CO<sub>3</sub> core-shell materials have been shown to exhibit water splitting capabilities for H<sub>2</sub> production [25–28]. Likewise, ZnO/MgAl-CO<sub>3</sub> composites have been used for the photodegradation of dyes such as Malachite Green and Methylene Orange [29,30]. By altering the LDH in composites from MgAl-CO<sub>3</sub> to ZnCr-CO<sub>3</sub> type, magnetic core-shell composites have also been applied to adsorption and photocatalysis of methylene blue [31]. To produce core-shell materials, reactions have been typically carried out in multi-step processes, either by hydrothermal or co-precipitation reactions. Two-step synthesis methods for core-shell composite materials can be time consuming and to the knowledge of the authors, there have been no attempts to incorporate both reactions into a single process.

The aim of this research was to produce ZnO@Mg<sub>2</sub>Al-CO<sub>3</sub> core-shell nanomaterials via a once through continuous hydrothermal synthesis method, negating the need for multiple step processes. This continuous hydrothermal method has been utilised for the controlled synthesis of both metal oxides and LDHs (Dunne et al., 2015; Clark et al., 2018) individually and was used as a framework to design a system where rapid synthesis of both the ZnO core and LDH shell could be achieved in a single step.

## 2. Materials and Methods

### 2.1. Reagents and Chemicals

All chemicals for precursor solutions were reagent grade and were used as received. Aluminium nitrate (Al(NO<sub>3</sub>)<sub>3</sub>·9H<sub>2</sub>O ≥ 99%) and were purchased from Acros Organics (Geel, Belgium). Sodium carbonate (Na<sub>2</sub>CO<sub>3</sub> ≥ 99%), zinc nitrate (Zn(NO<sub>3</sub>)<sub>2</sub>·2H<sub>2</sub>O ≥ 98%), magnesium nitrate (Mg(NO<sub>3</sub>)<sub>2</sub>·6H<sub>2</sub>O ≥ 98%), and sodium hydroxide (NaOH ≥ 98%) were purchased from Sigma Aldrich (Dorset, United Kingdom). Prior to synthesis, fresh solutions were prepared by dissolving metal salts in deionised water.

### 2.2. Preparation of Composite Nanomaterials

Attempted continuous hydrothermal synthesis (CWS) of composite nanomaterials was carried out in a sequential reaction system that combines two counter current flow reactors (University of Nottingham, Nottingham UK). The counter current reactor design is detailed elsewhere [32]. The first reactor is used to produce the ZnO core, and the second is used to produce the LDH shell. For synthesis Zn(NO<sub>3</sub>)<sub>2</sub>·6H<sub>2</sub>O (0.05 M) was fed at ambient temperature, in the up-flow to the first reactor at 10 mL min<sup>-1</sup>, while a solution of NaOH (0.05 M) was heated to 350 ± 5 °C and fed in the down-flow at 20 mL min<sup>-1</sup>. The outflow was then cooled in a heat exchanger before NaOH (0.15 M) and Na<sub>2</sub>CO<sub>3</sub>

(0.017 M) was fed into the flow, via a third pump again at  $10 \text{ mL min}^{-1}$ . This mixed feed was heated to  $100 \pm 3 \text{ }^\circ\text{C}$  in the down-flow into the second reactor. LDH metal salts were pumped into the up-flow for the second reactor, at ambient temperature, at  $20 \text{ mL min}^{-1}$ . The reaction is outlined in a simplified schematic (Figure 1). Reaction pressure for the whole system was maintained at 240 bar by a Back Pressure Regulator (Pressure Tech, Hadfield, UK). Samples were centrifuged and washed thoroughly. Following washing samples were freeze-dried. To compare the composite  $\text{ZnO@Mg}_2\text{Al-CO}_3$  (labelled  $\text{ZnO-LDH}$ ) with the pure materials, separate  $\text{ZnO}$  and  $\text{Mg}_2\text{Al-CO}_3$  materials were also synthesised.

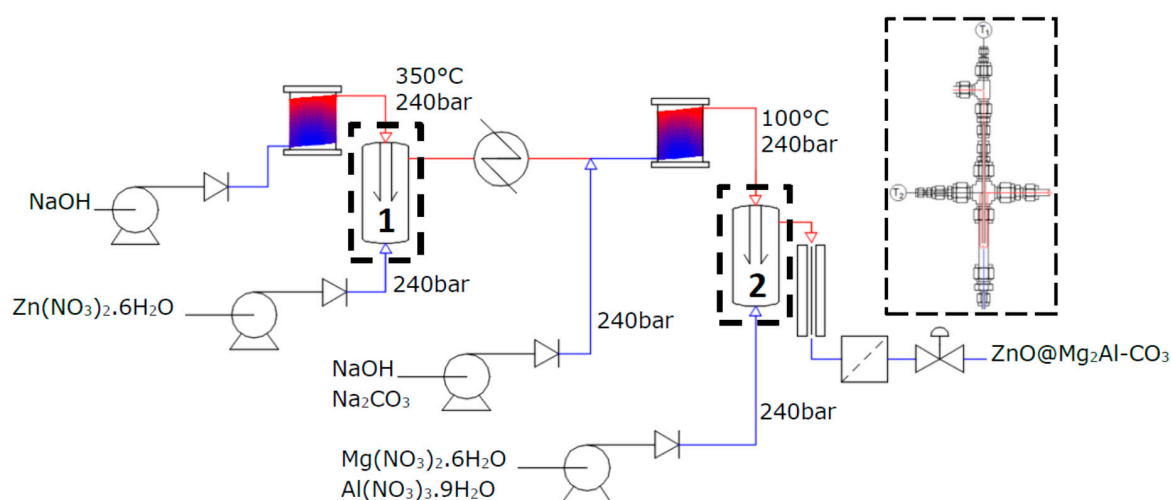


**Figure 1.** Simplified reaction schematic for sequential counter current flow system with reactor 1 and reactor 2 labelled 1 and 2, respectively.

Reactors 1 and 2 consisted of a  $1/8''$  tube inside a  $3/8''$  tube and a  $1/4''$  tube inside a  $1/2''$ , respectively. The increase in the inner tube diameter in reactor 2 was necessary to prevent blockages at the nucleation point at the outlet of the inner tube as a result of solid particles flowing in from reactor 1. A series of other experiments were carried out to investigate the influence of flow rates in the two reactors and the potential for unreacted precursors from the first reactor influencing the products forming in the second reactor. The variation in reactor geometry and flow rates between reactor 1 and reactor 2 system result in changes to the Reynolds number and mixing regime between the first and second reactors. Any variation in LDH synthesis between reactor 1 and reactor 2, as a result of increased flow rate and changes to reactor geometry, were examined through changes in material characteristics.  $\text{Mg}_2\text{Al-CO}_3$  was produced at  $60 \text{ mL min}^{-1}$  with deionised water flowing from reactor 1 and LDH precursors flowing into reactor 2. The precursor concentrations were altered to accommodate the change in flow rate and so the ratio of  $\text{OH}^-$  to  $\text{M}^{\text{II}} + \text{M}^{\text{III}}$  was kept at 2.5. The effect of residual counter ions from the synthesis of  $\text{ZnO}$  (Unreacted  $\text{NO}_3^-$  and  $\text{Zn}^{2+}$ ) were also investigated using the dual reactor setup with synthesis of  $\text{Mg}_2\text{Al-CO}_3$  only occurring in the second reactor. Table 1 and Figure S1 in Supplementary information outline the details of the full matrix of synthesis experiments.

**Table 1.** Synthesis conditions for layered double hydroxides (LDHs) and composite.

Sample	Reactor	Material	[NaOH] (mol L <sup>-1</sup> )	Down-Flow (mL min <sup>-1</sup> )	[M <sup>II</sup> + M <sup>III</sup> ] (mol L <sup>-1</sup> )	Up-Flow (mL min <sup>-1</sup> )
ZnO	1	ZnO	0.050	20	0.05	10
LDH <sub>initial</sub>	1	Mg <sub>2</sub> Al-CO <sub>3</sub>	0.125	20	0.10	10
<sup>†</sup> LDH <sub>mix</sub>	-	mixture of ZnO and LDH <sub>initial</sub>	-	-	-	-
ZnO-LDH	1	ZnO	0.05	40	0.05	20
	2	Mg <sub>2</sub> Al-CO <sub>3</sub>	0.15		0.05	
LDH-only experiments						
LDH3	2	Mg <sub>2</sub> Al-CO <sub>3</sub>	0.25	40	0.05	20
* LDH4	2	Mg <sub>2</sub> Al-CO <sub>3</sub>	0.15	40	0.05	20
LDH5	2	Mg <sub>2</sub> Al-CO <sub>3</sub>	0.15	40	0.05	20
LDH6	2	Mg <sub>2</sub> Al-CO <sub>3</sub>	0.25	40	0.05	20
LDH7	2	Mg <sub>2</sub> Al-CO <sub>3</sub>	0.15	40	0.05	20
LDH8	2	Mg <sub>2</sub> Al-CO <sub>3</sub>	0.25	40	0.05	20

\* Recovered reaction liquor from ZnO synthesis used to flow through reactor 1. <sup>†</sup> Dry ZnO/LDH<sub>initial</sub> powders mixed at 23%:77% ratio of ZnO:LDH.

### 2.3. Materials Characterisation

X-ray diffraction (XRD) of powder samples was carried out on a Bruker D8-Advance Diffractometer (Bruker, Billerica, MA, USA) using Cu K $\alpha$  radiation ( $\lambda = 0.15418$  nm) between 5° and 70° 2 $\theta$ , at a rate of 0.75° min<sup>-1</sup>. Crystal domain lengths were calculated using the Scherrer equation. Scanning Electron Microscopy with Energy Dispersive Spectroscopy (SEM-EDS) was used to establish composition of ZnO-LDH; prior to analysis, samples were pelleted and carbon-coated to produce a flat surface. Analysis was performed using a Siemens XL30 SEM (Siemens, Munich, Germany) with a tungsten filament. Specific surface area and pore size distribution were analysed using nitrogen adsorption at 77 K with a Micromeritics Tristar II 3020 (Micromeritics, Atlanta, GA, USA). The Brunauer–Emmett–Teller (BET) and Barrett–Joyner–Halenda (BJH) methods were used to calculate surface and pore size distribution. Samples were dispersed onto copper supported lacy carbon films (Agar Scientific) and a JEOL 2000FX (JEOL UK, Welwyn Garden City, UK) transmission electron microscope (TEM) was used to image particles with acceleration voltage at 200 kV. Image analysis of 100–200 individual particles from these TEM micrographs were then used to calculate average particle size and particle size distribution. These data were compared against the crystal domain length (CDL) calculated from the Scherrer equation. Photo-activity of materials was examined using a Cary 300 Ultraviolet-Visible (UV-Vis) spectrophotometer (Agilent, Stockport, UK), scanning between 800 nm and 200 nm. Thermal stability was assessed on a TA Q500 TGA instrument (TA Instruments, Elstree, UK). Analysis heating rate was 5 °C min<sup>-1</sup> between 25 °C and 700 °C under N<sub>2</sub> flow at 40 mL min<sup>-1</sup>. The conversion rate of Zn<sup>2+</sup> to ZnO in reactor 1 experiments was measured via atomic absorption spectroscopy (AAS) (after removing ZnO particles from the product slurry using a centrifuge) using a Perkin Elmer 272 Atomic Adsorption Spectrophotometer with a Zn hollow cathode lamp ( $\lambda = 213.9$ ).

## 3. Results and Discussion

### 3.1. Crystal Characterisation of Composite and Single-Phase Materials

Pure phase Mg<sub>2</sub>Al-CO<sub>3</sub> exhibits R $\bar{3}m$  rhombohedral crystal symmetry, whereas ZnO exhibits P6<sub>3</sub>mc symmetry. The diffraction pattern for ZnO-LDH shows reflections for both ZnO and Mg<sub>2</sub>Al-CO<sub>3</sub>

phases (Figure 2), indicating either formation of ZnO-LDH or a mix of both ZnO and  $Mg_2Al-CO_3$  phases. The relative intensity of LDH reflections in the ZnO-LDH pattern suggests a more crystalline hydrotalcite phase in the proposed composite material when compared with  $LDH_{initial}$ , this is not the case with the ZnO, as there are no changes in relative reflection intensity between the ZnO and ZnO-LDH diffractogram. The lattice parameters (Table 2) show slight variation between pure materials and the composites. However, the discrepancy is minimal, and the lattice parameters generally correspond well with values in literature [33–37].

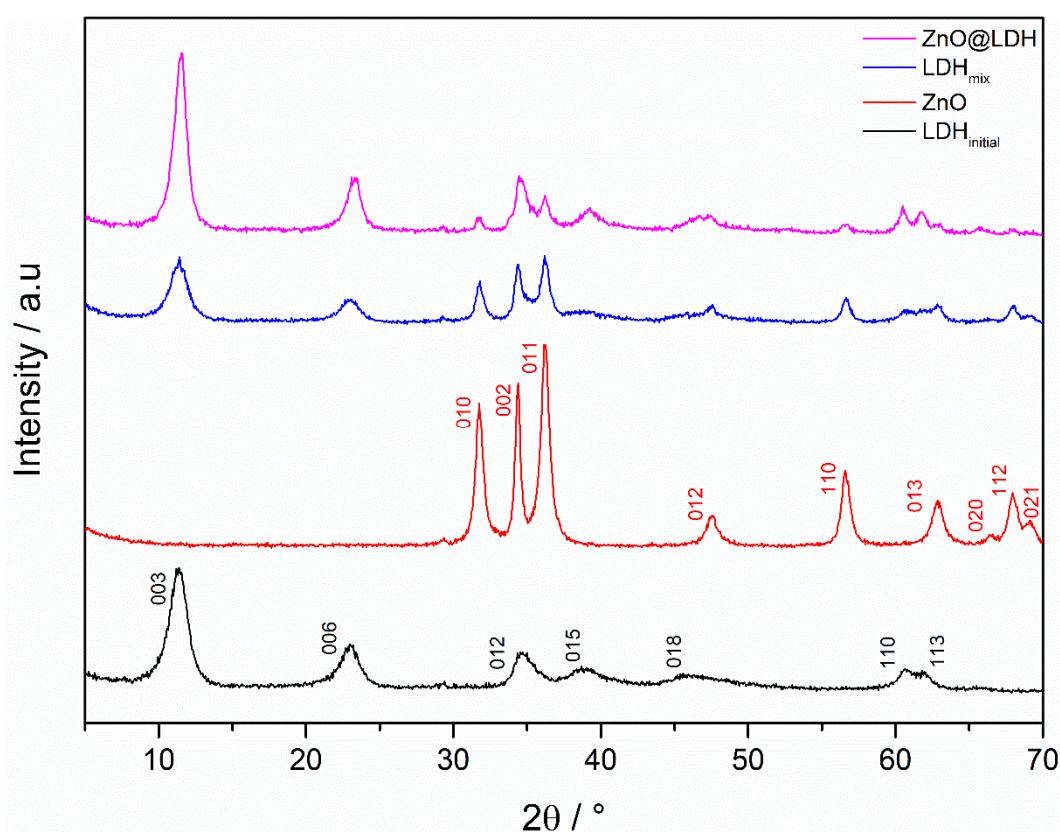


**Figure 2.** X-ray diffractograms for ZnO@LDH, ZnO and  $Mg_2Al-CO_3$  produced in reactor 1 ( $LDH_{initial}$ ) and a mix of  $LDH_{initial}$  and ZnO ( $LDH_{mix}$ ).

**Table 2.** Lattice parameters of pure and composite materials.

Sample	Miller Indices	<sup>a</sup> Lattice Parameter a (nm)	Miller Indices	<sup>a</sup> Lattice Parameter c (nm)
ZnO	010	0.33	002	0.52
$LDH_{initial}$	110	0.30	003	2.32
ZnO-LDH	010	0.32 <sup>a</sup>	002	0.52 <sup>a</sup>
	110	0.31 <sup>b</sup>	003	2.28 <sup>b</sup>

<sup>a</sup> Lattice parameters for ZnO phase. <sup>b</sup> Lattice parameters for  $Mg_2Al-CO_3$  phase.

Crystal domain length (CDL) approximated from the Scherrer equation (Table 3) indicates differences between single phase profiles and those in the composite. The average crystallite size of the ZnO phase in the composite material is significantly larger than in single phase ZnO (42 nm from 25nm, respectively). Crystal size of the LDH phase in the composite is marginally larger than that of  $LDH_{initial}$ . The larger ZnO CDL in ZnO-LDH may be due to the fact that some  $Zn^{2+}$  remains unconverted following the first reaction. Elemental analysis of reaction liquor indicates that conversion of  $Zn^{2+}$  to ZnO is approximately  $94 \pm 1\%$ . The remaining  $Zn^{2+}$  may then enable existing ZnO particles to grow further.



**Table 3.** Crystal domain length and particle size of ZnO, Mg<sub>2</sub>Al-CO<sub>3</sub> (LDH<sub>initial</sub>), and ZnO-LDH composite.

Sample	XRD			TEM	
	CDL (012) (nm)	CDL (003) (nm)	CDL (110) (nm)	<sup>b</sup> Particle Size (nm)	<sup>b</sup> Particle Size (nm)
ZnO	25	-	-	22 ± 14	-
LDH <sub>initial</sub>	-	8	25	-	34 ± 34
ZnO-LDH	42	12	27	53 ± 40	51 ± 22

<sup>b</sup> Average particle size from TEM micrographs with standard deviation of from Gaussian distribution ( $n = 3$ ).

Electron microscope images in Figure 3 outline the differences between the three materials under scrutiny. The LDH platelets shown in Figure 3c are less defined in terms of shape, compared with the ZnO nanoparticles with a significant degree of agglomeration and stacking (Figure 3d). The Mg<sub>2</sub>Al-CO<sub>3</sub> platelets in the ZnO-LDH sample appear to exhibit less face stacking than the platelets in the LDH<sub>initial</sub> sample. There are also rods visible in the SEM micrograph in Figure 3f. There are larger LDH platelets evident from TEM in the ZnO-LDH sample compared with LDH<sub>initial</sub>, and the CDL for (110) reflection is also slightly larger. The increase in size of crystals may be due to a growth-dominated reaction. Platelets first nucleated using ZnO as seed points then grow preferentially rather than nucleate to form new platelets. Having said this, the differences in CDL for LDH platelets between LDH<sub>initial</sub> and ZnO-LDH could equally be as a result of the changes in flow rates of synthesis, affecting the Reynolds numbers and mixing regime. ZnO crystals are significantly larger in both XRD and TEM in the composite materials compared to the pure ZnO due to continued growth from unreacted Zn<sup>2+</sup> as well as Ostwald ripening inside the second reactor. The TEM micrograph in Figure 3e shows a large rod particle surrounded by Mg<sub>2</sub>Al-CO<sub>3</sub> platelets. The micrograph might indicate that the formation of a composite material has been achieved, as a result of areas of high pH within the reaction system. The higher pH (> 10) led to a negative zeta potential on the ZnO allowing an electrostatic attraction to form between the ZnO and Mg<sub>2</sub>Al-CO<sub>3</sub> [17,38].

### 3.2. Specific Surface Area Analysis

Type-IV shape isotherms can be identified in Figure 4 for all materials. The ZnO isotherm demonstrates a H1 type hysteresis loop, indicating meso-porosity with ink bottle pore shapes, which is most likely to arise from the agglomeration of the ZnO (Figure 3a). From the S<sub>BET</sub> analysis of the isotherms (Table 4), the ZnO-LDH appears to have a higher specific surface area than either pure phase material (ZnO and LDH<sub>initial</sub>) or the artificial mix of the two pure materials (LDH<sub>mix</sub>). TEM and SEM images (Figure 3) show some 3D structuring in the ZnO-LDH sample (Figure 3f), which is less evident in LDH<sub>initial</sub> (Figure 3d). The LDH<sub>initial</sub> samples appears to exhibit large block-like particles with distinct flat sheets. The more open 3D structure of the platelets in the ZnO-LDH (resulting from edge-face connections), gives rise to a H1 hysteresis loop indicating that there are some aggregated LDH platelets present in the sample [39]. The LDH<sub>initial</sub> shows more face-face stacking in material, which might explain the H2 and H3 hysteresis profile in the LDH<sub>initial</sub> isotherm. The sharp desorption branch is associated with H2 hysteresis and the inclined tail at high P/P<sub>0</sub> found in H3 loops. This is to be expected as H3 hysteresis is associated with aggregation of platelet-like particles and clays [39]. It is also worth noting that there is a significant difference between the ZnO-LDH and LDH<sub>mix</sub> (the mix of separate samples of LDH and ZnO) isotherm types. The isotherm for LDH<sub>mix</sub> shows a similar profile to those given by the ZnO and LDH<sub>initial</sub> samples. These differences in profile, specific surface areas from BET, and pore volume (Table 4) suggest that ZnO-LDH is a genuine composite material rather than a binary mix of discrete ZnO and Mg<sub>2</sub>Al-CO<sub>3</sub> particles.

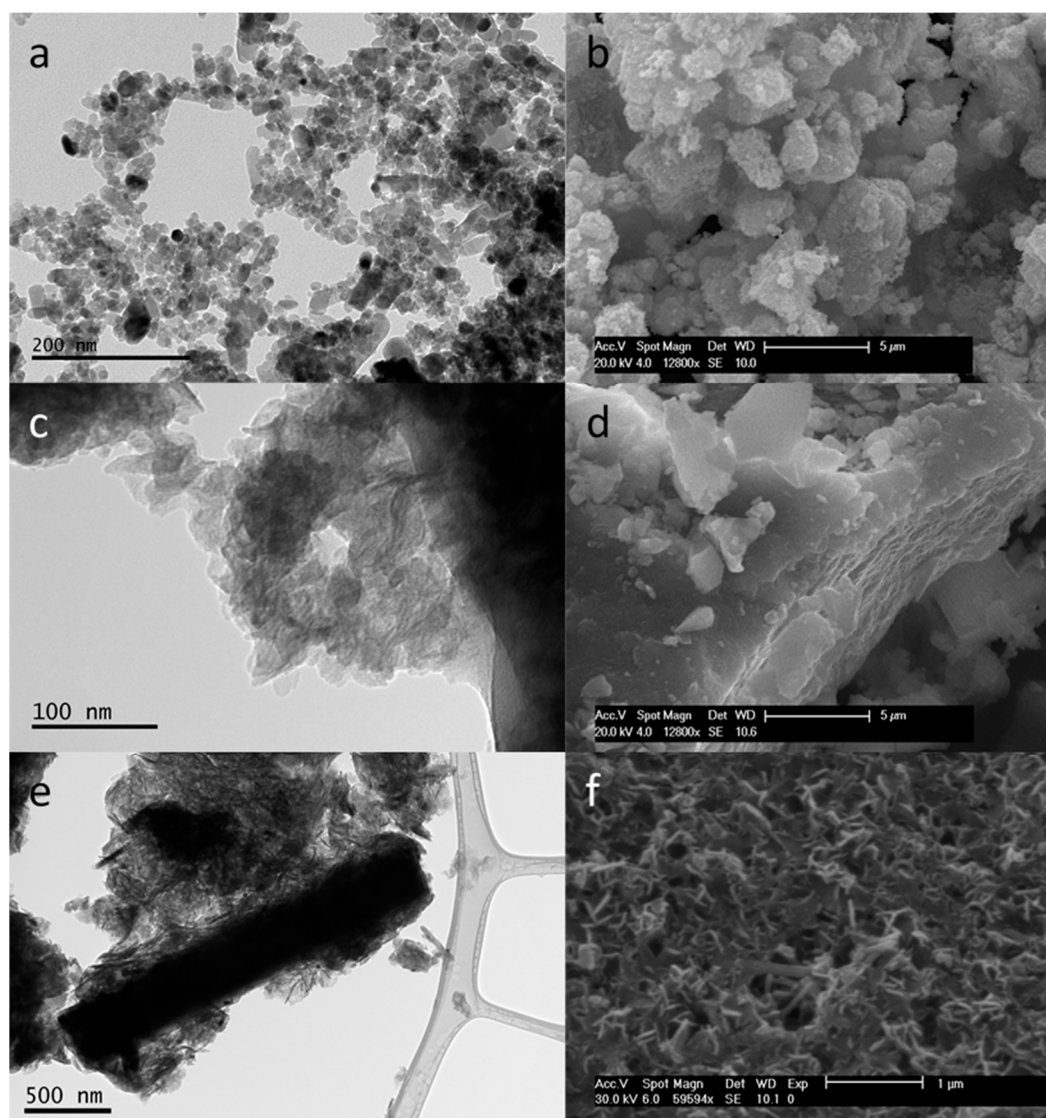


**Figure 3.** Transmission electron microscopy images (200 kV and  $\times 150,000$ – $500,000$  magnification) (a) ZnO, (c) LDH<sub>initial</sub>, (e) ZnO-LDH and SEM micrographs (b) ZnO, (d) LDH<sub>initial</sub>, (f) ZnO-LDH.

**Table 4.** Specific surface area, pore diameter, and cumulative pore volume of ZnO, Mg<sub>2</sub>Al-CO<sub>3</sub> (LDH<sub>initial</sub>), ZnO-LDH composite, and a mix of ZnO and LDH<sub>initial</sub> (LDH<sub>mix</sub>).

Sample	S <sub>BET</sub> (m <sup>2</sup> g <sup>-1</sup> )	Pore Diameter (nm)	Pore Volume (cm <sup>-3</sup> g <sup>-1</sup> )
ZnO	53.0 ± 0.1	17.6	0.3
LDH <sub>initial</sub>	58.2 ± 0.3	4.0	0.1
LDH <sub>mix</sub>	39.6 ± 0.1	7.2	0.1
ZnO-LDH	76.2 ± 0.1	17.0	0.7

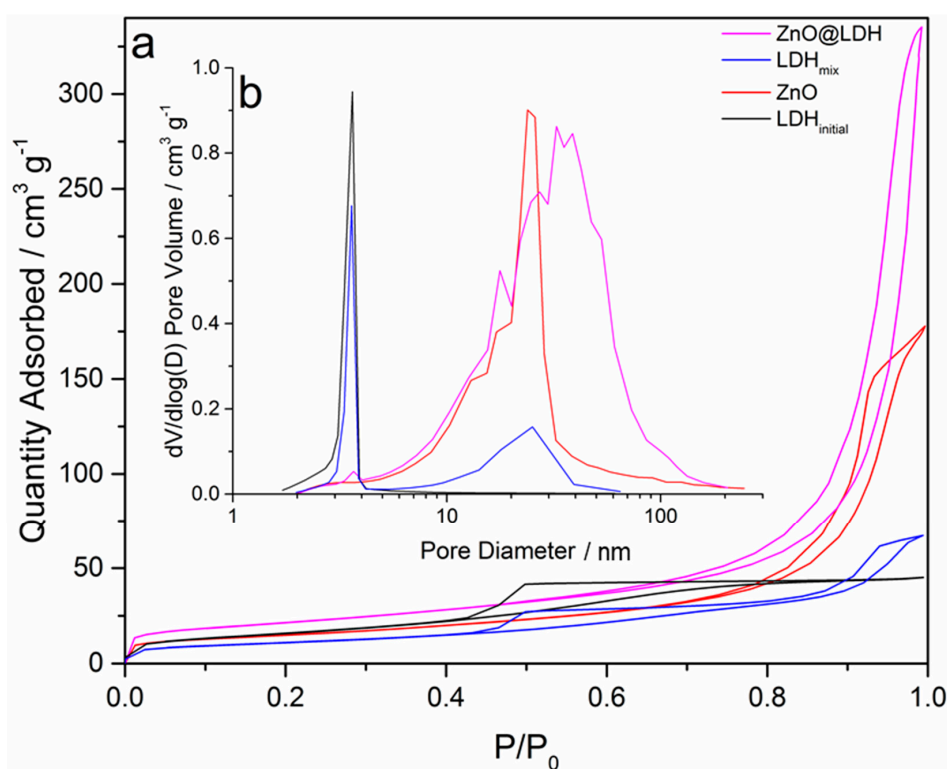


**Figure 4.** (a) Type-IV isotherms, (b) pore size distribution for ZnO@LDH composite, ZnO, Mg<sub>2</sub>Al-CO<sub>3</sub> (LDH<sub>initial</sub>), and a dry mix of ZnO and LDH<sub>initial</sub> (LDH<sub>mix</sub>).

### 3.3. Chemical Characterisation

The molecular ratio of magnesium to aluminium was calculated using SEM-EDS analysis (Figure S2a–d, Table S1) and was found to be 1.97 for LDH<sub>initial</sub>. This value is close to the Mg<sup>2+</sup>/Al<sup>3+</sup> ratio in the precursor solutions. However, the Mg/Al ratio in the composite material was found to be 1.27 using SEM-EDS analysis. This change indicates a lower conversion of Mg<sup>2+</sup> in the composite compared to the LDH. This can be seen in Figure S2c,d; the intensity of the EDX peaks in Figure S2c indicate approximately a 2:1 ratio of counts for magnesium to aluminium, however the same peaks in Figure S2d show that the levels of Mg and Al were similar. The reduced NaOH in the synthesis of ZnO-LDH flowing into the second reactor could cause the reduced Mg<sup>2+</sup>/Al<sup>3+</sup> ratio. Unreacted Zn<sup>2+</sup> may also react in the presence of OH<sup>−</sup> and Al<sup>3+</sup> to produce Zn<sub>x</sub>Al-CO<sub>3</sub>, which is the most likely cause of the reduced Mg<sup>2+</sup> conversion. The unreacted Zn<sup>2+</sup> (in the precursor) is approximately 6%, determined by atomic absorption spectroscopy, on the reaction liquor from ZnO synthesis. This low amount of unreacted Zn<sup>2+</sup> may contribute to the formation of Zn<sub>2</sub>Al-CO<sub>3</sub> LDH that would unlikely be detectable during XRD analysis. It is also possible that ZnO particles in the reactor down-flow may partially re-dissolve, as a result of increased temperature and reduced pH of the solution when the LDH metal salts are added to the second reactor [40]. This would allow Zn<sup>2+</sup> in the reactor to form Zn<sub>x</sub>Al-CO<sub>3</sub>. Increasing the NaOH content in reactor 2 by increasing the concentration in feed stream 3, which is after the first reactor but before the second heater (Figure 1), could resolve this issue, as the addition of more NaOH would not increase the conversion of Zn<sup>2+</sup> to ZnO, but it would reduce any dissolution of the ZnO. However, it is possible that it would lead to greater precipitation of Mg<sup>2+</sup> [41] and nucleation and growth rates of the LDH in the second reactor.

### 3.4. Thermal Stability

With LDH decomposition, there are three distinct mass loss events, dependant on LDH type. These mass loss events correspond to the peaks denoted in a dW/dT plot:



- (a) The loss of surface bound moisture (<100 °C) [42].
- (b) The bound interlayer water (100–200 °C) [43].
- (c) The breakdown of the layered structure and loss of interlayer anion (in this case -CO<sub>3</sub> to the oxide and CO<sub>2</sub>) [44].

These samples were dried prior to analysis, which means that the first peak is not particularly obvious. The TGA mass loss profile for the ZnO-LDH sample is significantly different from the pure ZnO, LDH<sub>initial</sub> and LDH<sub>mix</sub> samples (Figure 5a). There is a pronounced peak around 150 °C that is evident in the ZnO-LDH profile but not the others. In principle, this peak should be visible in one of the, ZnO or Mg<sub>2</sub>Al-CO<sub>3</sub>, constituent materials components. However, the peak is evident in the mass loss profile for Zn<sub>2</sub>AlCO<sub>3</sub> LDH. Zn<sub>2</sub>AlCO<sub>3</sub> has a less well defined third peak around 220 °C, which is smaller and at a lower temperature than the peaks at 375 °C seen in the LDH<sub>initial</sub> and 320 °C with the ZnO-LDH sample (Figure 5b). A Zn<sub>2</sub>Al-CO<sub>3</sub> LDH was produced as part of other synthesis work relating to continuous LDH synthesis [40].

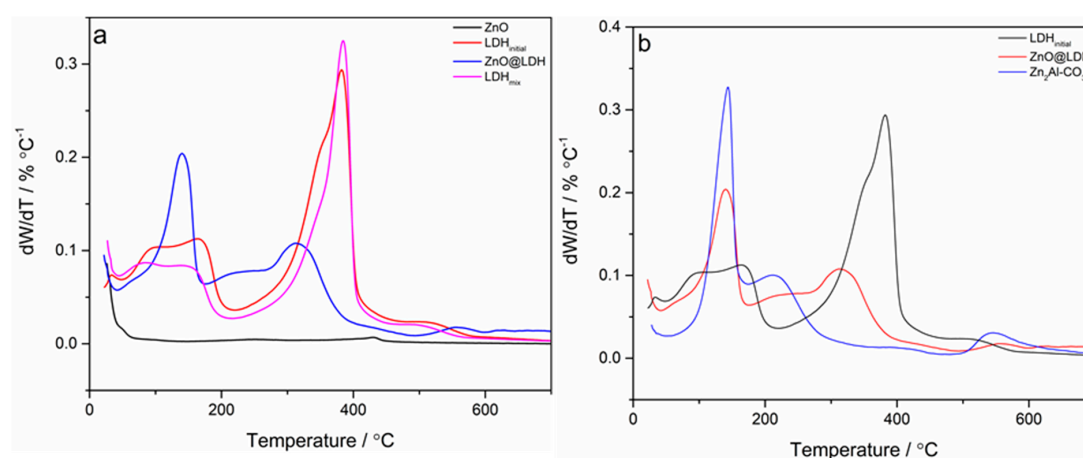


**Figure 5.** Derivative thermal decomposition of (a) ZnO, LDH<sub>initial</sub>, LDH<sub>mix</sub>, and ZnO-LDH (b) Zn<sub>2</sub>Al-CO<sub>3</sub> ZnO-LDH and LDH<sub>initial</sub>. All samples heated to 700 °C with a rate of 5 °C min<sup>-1</sup> 40 mL min<sup>-1</sup> flow rate of N<sub>2</sub>.

The breakdown of the lamella structure and consequent mass loss of interlayer anions in ZnO-LDH suggests the thermal stability is of the layered double hydroxide within the ZnO-LDH composite is somewhat less than the LDH. This is possibly due to the presence of Zn<sub>x</sub>Al-CO<sub>3</sub> and a compromised Mg<sub>2</sub>Al-CO<sub>3</sub> LDH structure, arising from a lower Mg/Al ratio. This might also be caused (to some extent) by the smaller particle size of the LDH component in the ZnO-LDH sample. The total mass loss of the ZnO-LDH during heating was 37%, whereas the mass loss of the LDH was 47% and ZnO was 3%. The mass loss of the composite material indicates that the mass fraction of the LDH in the composite is approximately 0.77. This value is based on theoretical mass loss based on combining single phase ZnO and pure LDH1 at different ratios. The mass fraction of LDH derived from the TGA profile was larger than the mass fraction given by the SEM-EDS analysis. This may be in part due to the presence of Zn<sub>x</sub>Al-CO<sub>3</sub> in the composite material.

### 3.5. Electronic Structure Characterisation

Direct transitions were found for all three materials tested using the Tauc equation and the UV profiles (Figure S3 in ESI). The composite material shows a slight increase in band gap energy compared with the ZnO (Table 5), meaning that a lower wavelength of light, and more energy, is necessary for electron transition to occur. LDH<sub>initial</sub> has a band gap energy of 5.24 indicating poor semiconducting characteristics. The other three are relatively similar.

**Table 5.** Band gap energy of the components and hybrid structure.

Sample	Band Gap (eV)
ZnO	3.21
LDH <sub>initial</sub>	5.24
LDH <sub>mix</sub>	3.22
ZnO-LDH	3.31

### 3.6. The Impact of Reactor 1 vs. Reactor 2

Several experiments were undertaken to understand the influence of secondary production of the LDH material and the presence of the ZnO in the inlet flow to reactor 2. It is worth noting that the LDH<sub>initial</sub> itself was manufactured in reactor one using the standard flow conditions 20 mL min<sup>-1</sup> down flow and 10 mL min<sup>-1</sup> up flow. As such, the LDH<sub>mix</sub> and ZnO are also products from reactor 1. As such, these experiments were specifically to “deconstruct” the processes at work in the cascaded reactor set up where ZnO is manufactured in the first reactor and LDH is manufactured in the second.

### 3.7. LDH Formation in Reactor 1 and in Reactor 2

The main difference between the two reactors is the mixing dynamics, which is more turbulent in reactor 2 (albeit still laminar), compared to reactor 1 (see Table 6). This suggests that immediately after the initial mixing of the down-flow and up-flow streams, mixing is reduced to a greater extent in reactor 1 than in reactor 2. The changes in flow regime appear to have a small impact on the diffraction pattern of LDH<sub>initial</sub> and LDH3 (Figure S4 in ESI), with LDH<sub>initial</sub> showing more defined reflections. This is unsurprising considering the small difference in Reynolds numbers. The CDL of the samples appears to be impacted slightly by the change in Reynolds number as the CDL in the (110) plane is increased by 5nm from LDH<sub>initial</sub> to LDH3 (Table 6).

**Table 6.** Changes to crystal domain length (CDL) and Reynolds number in reactors 1 and 2.

Sample	Reactor	Flow Rate (mL min <sup>-1</sup> )	Re	CDL (003) (nm)	CDL (110) (nm)
LDH <sub>initial</sub>	1	30	235	8	25
LDH3	2	60	297	7	30

The more turbulent flow regime in reactor 2 appears to have a significant negative effect on specific surface area ( $S_{BET}$  is reduced to <5 m<sup>2</sup> g<sup>-1</sup> for LDH3). The cause of this is unclear, however it may be due to previously unreacted OH<sup>-</sup> causing a greater degree of agglomeration and stacking in the sample due to the increased mixing occurring across the length of the reactor. It is unlikely that the marginal increase in CDL has caused the dramatic decrease in  $S_{BET}$  and pore volume (Table 7). LDH3 exhibits a more defined “block-sheet” type structuring with no visible faults or porous structures (Figure S5 in ESI), but this does not directly explain the drop in specific surface area.

**Table 7.** Specific surface area ( $S_{BET}$ ) and pore characteristics of Mg<sub>2</sub>Al-CO<sub>3</sub> LDH synthesised from reactors 1 and 2.

Sample	$S_{BET}$ (m <sup>2</sup> g <sup>-1</sup> )	BJH (Barrett, Joyner, and Halenda) Pore Diameter (nm)	BJH Pore Volume (cm <sup>3</sup> g <sup>-1</sup> )
LDH <sub>initial</sub>	58.2 ± 0.3	3.5	0.07
LDH3	20.1 ± 0.1	4.2	0.04

### 3.8. The Impact of Residual Ions from ZnO Synthesis

As discussed earlier, the conversion of Zn<sup>2+</sup> to ZnO in reactor 1 was approximately 94%. This equates to 72 ± 6mg L<sup>-1</sup> of unreacted Zn<sup>2+</sup>. There is also the NO<sub>3</sub><sup>-</sup> counter ion from the Zn

precursor in the reaction liquor that is used to produce the ZnO-LDH composite. Diffractograms show decreased crystallinity for samples produced with lower NaOH concentration (Figure S6). The lower crystallinity is caused by disruption in the layered structure by the reduced  $\text{Mg}(\text{OH})_2$  (Table 8). This would suggest that, as a higher crystallinity is observed for ZnO@LDH compared to  $\text{LDH}_{\text{initial}}$  (Figure 2), a lower NaOH concentration in reactor 2 is unlikely to be the cause of the lower  $\text{Mg}^{2+}/\text{Al}^{3+}$  ratio observed in SEM-EDS analysis. The CDL outlined in Table 9 indicates only a marginal increase with the samples produced at increased NaOH conditions. Residual  $\text{Zn}^{2+}$  ions appear to have little effect on the crystal structure because the concentration in the feed is so low. Nitrate also appears to have no effect on the structure of the samples. The effect of added  $\text{NO}_3^-$  from  $\text{Zn}(\text{NO}_3)_2 \cdot \text{H}_2\text{O}$  has the same effect as the  $\text{NO}_3^-$  from the LDH metal salts. Carbonate ions will preferentially form in the interlayer region due to the higher charge density [45], therefore regardless of the presence of additional nitrate in reactor 2, no changes were observed.

**Table 8.** Scherrer approximation of crystal domain length (CDL).

Sample	CDL (003)/nm	CDL (110)/nm
LDH4	6	25
LDH5	6	26
LDH6	7	25
LDH7	5	27
LDH8	8	27

**Table 9.** Specific surface area (SBET) and pore size for samples isolating residual ions from ZnO synthesis.

Sample	$S_{\text{BET}}$ ( $\text{m}^2 \text{g}^{-1}$ )	Pore Diameter (nm)	Pore Volume ( $\text{cm}^3 \text{g}^{-1}$ )
LDH4	$266.8 \pm 0.4$	16.85	1.36
LDH5	$270.2 \pm 0.5$	15.87	1.29
LDH6	$22.6 \pm 0.1$	3.89	0.06
LDH7	$271.7 \pm 0.5$	14.55	1.20
LDH8	$26.1 \pm 0.2$	4.42	0.05

From Table 9, the specific surface area and morphology of LDHs does not appear to be affected by the residual  $\text{Zn}^{2+}$  or  $\text{NO}_3^-$  (from the simulated ZnO synthesis experiments). However, the concentration of NaOH, in the second stage, does have a significant impact. Samples produced with higher concentration of NaOH (LDH6 and LDH8) show lower specific surface area than  $\text{LDH}_{\text{initial}}$  and significantly lower specific surface area than LDH5 and LDH7. Table 1 illustrates the synthesis conditions for the respective LDHs, and it appears that reducing the NaOH concentration to a concentration that matches the  $\text{OH}^-/(\text{M}^{\text{II}} + \text{M}^{\text{III}})$  ratio of 1.5 rather than 2.5 causes a dramatic increase in specific surface area. This can be linked to changes in the morphology of the LDH samples. LDH5 exhibits a more fragmented structure consisting of smaller agglomerates with more gaps between them, whereas LDH6 has the more typical structure seen from the continuous synthesis of  $\text{Mg}_2\text{Al-CO}_3$  LDHs. Agglomeration and stacking produce a block-like structure of large sheets, which cause the reduced specific surface area compared with the LDH produced at lower NaOH concentration. Specific surface area appears to be affected more by agglomeration and stacking of platelets rather than by crystal size. The reduced NaOH concentration in the feed to the second reactor causes a reduction in  $\text{Mg}(\text{OH})_2$  precipitation in the LDH  $\text{Mg}(\text{OH})_2$  typically precipitates at higher pH ranges than  $\text{Al}(\text{OH})_3$  and  $\text{Zn}(\text{OH})_2$  [41]. The concentration of  $\text{Zn}(\text{OH})_2$  is negligible in the sample prepared using  $\text{Zn}^{2+}$  reaction liquor (LDH4), but it is present however in small quantities in LDH7 and LDH8. However, there is no indication from Table 9 that the Zn has a significant impact on the physicochemical properties of the LDH. Total mass loss for LDH4, LDH7 and LDH8 was 48%, 47%, and 48%, respectively, during thermal decomposition (Figure S7 in ESI). The low mass loss in LDH7 is attributed to mass loss that is 1 to 2% lower for each

mass loss event compared with LDH4. The shape of the TGA profiles indicates a significant difference in thermal stability when the  $M^{II}/M^{III}$  ratio is disrupted, as a result of changes in NaOH concentration. Substantial mass loss due to the breakdown of the layered structure occurs between 300 and 400 °C for samples LDH6 and LDH8, which were produced with the higher NaOH concentration. Samples produced with lower NaOH content start to break down below 300 °C. Moisture loss is also a much more rapid process for samples LDH4, LDH5, and LDH7, occurring typically <100 °C. The changes in thermal stability are due to the disruption of the sheets, caused by the changes in  $M^{II}/M^{III}$  ratio, which weakens the overall structure of the LDH.

#### 4. Conclusions

The results obtained from this research suggest that, for the first time, a one-step continuous synthesis method of a core-shell ZnO-LDH composite material has been achieved. However, a pure two-phase composite material was not fully synthesised, as there was an indication of the presence of  $Zn_2Al-CO_3$ , as well as single phase ZnO and  $Mg_2Al-CO_3$  mixtures. The mass fraction of the LDH in the ZnO-LDH material was found to be approximately 0.77 from thermal decomposition studies. The relative Mg/Al ratio of the ZnO-LDH was reduced to 1.27 from the 1.97 seen in LDH<sub>initial</sub>. This change was due to the formation of  $Zn_2Al-CO_3$  LDH from residual  $Zn^{2+}$  ions unreacted from the first reactor and the dissolution of ZnO as a result of increased temperature and reduce pH in reactor 2. The lower NaOH reduced the formation of  $Mg(OH)_2$  in the second reactor significantly impacted the resultant  $M^{II}/M^{III}$  ratio. The CDL for the ZnO and ZnO-LDH were found to be 25 nm and 42 nm, respectively. The change in crystal size of ZnO was likely to be a result of the dissolution and re-precipitation of ZnO from smaller spherical particles into larger rod-shaped particles followed by some further precipitation of residual  $Zn^{2+}$  ions. The specific surface area of ZnO-LDH was higher than that of the single-phase powders, owing to the difference in the stacking arrangement between the single phase LDH and the LDH phase in the ZnO-LDH composite material. The open, “flower-like” pattern of LDH in the composite material allowed for a better adsorption capacity or adsorption rate compared to the single phase LDH. However, single-phase  $Mg_2Al-CO_3$  LDHs synthesised at a lower NaOH concentrations ( $OH^-/M^{II} + M^{III} = 1.5$ ) resulted in a significant increase in surface (to above  $250\text{ m}^2\text{ g}^{-1}$ ) regardless of the presence of any counter ions. More work is required to optimise the synthesis process (to ensure near-perfect coverage of the ZnO core with LDH platelets). In addition, their capability for adsorption and photodegradation of organic dyes should be explored.

**Supplementary Materials:** The following are available online at <http://www.mdpi.com/2079-4991/10/10/2052/s1>, Figure S1: Overview of all experiments, Figure S2: Scanning electron images (at a magnification of  $\times 100$ ) of (a) LDH<sub>initial</sub>, (b) ZnO-LDH and EDAX spectra, (c) LDH<sub>initial</sub>, (d) ZnO-LDH, Table S1: EDX spectra results outlining atomic and mass fractions of elements in ZnO-LDH composite, Figure S3: (a) UV-Vis DRS, (b) Kubelka–Munk plot, Figure S4: XRD patterns for  $MgAlCO_3$  made in reactor 1 and reactor 2, Figure S5: SEM micrographs depicting differences in microstructure and morphology between samples LDH<sub>initial</sub> (a, b) and LDH3 (c, d), Figure S6: Diffraction patterns for LDH samples LDH4-LDH8, Figure S7: Derivative mass loss profiles of LDHs produced with varying precursor ions and OH<sup>-</sup> concentration, Table S2: Weight fraction of metals in each LDH structure and residual metal content.

**Author Contributions:** Conceptualization, I.C.; investigation, I.C.; methodology, I.C.; analysis, I.C. and J.S.; supervision, E.L. and R.L.G.; writing—original draft, I.C.; writing—review, editing, and revisions, J.S. All authors have read and agreed to the published version of the manuscript.

**Funding:** The authors would like to acknowledge the EPSRC for providing scholarship funding through the University of Nottingham (EP/M5065881/1) and through the Centre for Doctoral Training in Sustainable Chemistry (EP/L015633/1). This work was also part funded through the European Union’s Seventh Framework Programme (FP7/2007–2013), grant agreement no. FP7-NMP4-LA-2012-280983, the SHYMAN project.

**Conflicts of Interest:** The authors declare no conflict of interest.

#### References

1. Auerbach, S.M.; Carrado, K.A.; Dutta, P.K. *Handbook of Layered Materials*; M. Dekker: New York, NY, USA, 2004; pp. 1–664.

2. Xu, R.; Pang, W.; Huo, Q. *Modern Inorganic Synthetic Chemistry*; Elsevier Science: Amsterdam, The Netherlands, 2011; pp. 1–590.
3. Bukhtiyarova, M.V. A review on effect of synthesis conditions on the formation of layered double hydroxides. *J. Solid State Chem.* **2019**, *269*, 494–506. [[CrossRef](#)]
4. Extremera, R.; Pavlovic, I.; Perez, M.R.; Barriga, C. Removal of acid orange 10 by calcined Mg/Al layered double hydroxides from water and recovery of the adsorbed dye. *Chem. Eng. J.* **2012**, *213*, 392–400. [[CrossRef](#)]
5. Lv, L.; He, J.; Wei, M.; Evans, D.G.; Duan, X. Factors influencing the removal of fluoride from aqueous solution by calcined Mg-Al-CO<sub>3</sub> layered double hydroxides. *J. Hazard. Mater.* **2006**, *133*, 119–128. [[CrossRef](#)]
6. Lv, L.; He, J.; Wei, M.; Evans, D.G.; Zhou, Z.L. Treatment of high fluoride concentration water by MgAl-CO<sub>3</sub> layered double hydroxides: Kinetic and equilibrium studies. *Water Res.* **2007**, *41*, 1534–1542. [[CrossRef](#)] [[PubMed](#)]
7. Lv, L.A.; Wang, W.; Wei, M.; Cheng, H.J. Bromide ion removal from contaminated water by calcined and uncalcined MgAl-CO<sub>3</sub> layered double hydroxides. *J. Hazard. Mater.* **2008**, *152*, 1130–1137. [[CrossRef](#)] [[PubMed](#)]
8. Khan, A.I.; Lei, L.X.; Norquist, A.J.; O'Hare, D. Intercalation and controlled release of pharmaceutically active compounds from a layered double hydroxide. *Chem. Commun.* **2001**, *22*, 2342–2343. [[CrossRef](#)]
9. Gao, Y.S.; Wu, J.W.; Wang, Q.; Wilkie, C.A.; O'Hare, D. Flame retardant polymer/layered double hydroxide nanocomposites. *J. Mater. Chem. A* **2014**, *2*, 10996–11016. [[CrossRef](#)]
10. Wang, Q.; Undrell, J.P.; Gao, Y.S.; Cai, G.P.; Buffet, J.C.; Wilkie, C.A.; O'Hare, D. Synthesis of Flame-Retardant Polypropylene/LDH-Borate Nanocomposites. *Macromolecules* **2013**, *46*, 6145–6150. [[CrossRef](#)]
11. Shao, M.F.; Han, J.B.; Wei, M.; Evans, D.G.; Duan, X. The synthesis of hierarchical Zn-Ti layered double hydroxide for efficient visible-light photocatalysis. *Chem. Eng. J.* **2011**, *168*, 519–524. [[CrossRef](#)]
12. Zhao, Y.F.; Li, B.; Wang, Q.; Gao, W.; Wang, C.L.J.; Wei, M.; Evans, D.G.; Duan, X.; O'Hare, D. NiTi-Layered double hydroxides nanosheets as efficient photocatalysts for oxygen evolution from water using visible Light. *Chem. Sci.* **2014**, *5*, 951–958. [[CrossRef](#)]
13. Alexandre, A.; Medina, F.; Rodriguez, X.; Salagre, P.; Cesteros, Y.; Sueiras, J.E. Cu/Ni/Al layered double hydroxides as precursors of catalysts for the wet air oxidation of phenol aqueous solutions. *Appl. Catal. B* **2001**, *30*, 195–207. [[CrossRef](#)]
14. Coq, B.; Tichit, D.; Ribet, S. Co/Ni/Mg/Al layered double hydroxides as precursors of catalysts for the hydrogenation of nitriles: Hydrogenation of acetonitrile. *J. Catal.* **2000**, *189*, 117–128. [[CrossRef](#)]
15. Zhang, H.; Pan, D.K.; Zou, K.; He, J.; Duan, X. A novel core-shell structured magnetic organic-inorganic nanohybrid involving drug-intercalated layered double hydroxides coated on a magnesium ferrite core for magnetically controlled drug release. *J. Mater. Chem.* **2009**, *19*, 3069–3077. [[CrossRef](#)]
16. Zhang, H.; Pan, D.K.; Duan, X. Synthesis, Characterization, and Magnetically Controlled Release Behavior of Novel Core-Shell Structural Magnetic Ibuprofen-Intercalated LDH Nanohybrids. *J. Phys. Chem. C* **2009**, *113*, 12140–12148. [[CrossRef](#)]
17. Chen, C.P.; Felton, R.; Buffet, J.C.; O'Hare, D. Core-shell SiO<sub>2</sub>@LDHs with tuneable size, composition and morphology. *Chem. Commun.* **2015**, *51*, 3462–3465. [[CrossRef](#)]
18. Chen, C.P.; Wang, P.H.; Lim, T.T.; Liu, L.H.; Liu, S.M.; Xu, R. A facile synthesis of monodispersed hierarchical layered double hydroxide on silica spheres for efficient removal of pharmaceuticals from water. *J. Mater. Chem. A* **2013**, *1*, 3877–3880. [[CrossRef](#)]
19. Chen, C.P.; Byles, C.F.H.; Buffet, J.C.; Rees, N.H.; Wu, Y.; O'Hare, D. Core-shell zeolite@aqueous miscible organic-layered double hydroxides. *Chem. Sci.* **2016**, *7*, 1457–1461. [[CrossRef](#)]
20. Guo, L.; Zhang, X.; Chen, Q.; Ruan, C.; Leng, Y. Enhanced removal performance by the core-shell zeolites/MgFe-layered double hydroxides (LDHs) for municipal wastewater treatment. *Environ. Sci. Pollut. Res.* **2016**, *23*, 6749–6757. [[CrossRef](#)] [[PubMed](#)]
21. Ning, F.Y.; Shao, M.F.; Zhang, C.L.; Xu, S.M.; Wei, M.; Duan, X. Co<sub>3</sub>O<sub>4</sub>@layered double hydroxide core/shell hierarchical nanowire arrays for enhanced supercapacitance performance. *Nano Energy* **2014**, *7*, 134–142. [[CrossRef](#)]
22. Li, X.; Yang, Z.C.; Qi, W.; Li, Y.T.; Wu, Y.; Zhou, S.X.; Huang, S.M.; Wei, J.; Li, H.J.; Yao, P. Binder-free Co<sub>3</sub>O<sub>4</sub>@NiCoAl-layered double hydroxide core-shell hybrid architectural nanowire arrays with enhanced electrochemical performance. *Appl. Surf. Sci.* **2016**, *363*, 381–388. [[CrossRef](#)]



23. Shao, M.F.; Ning, F.Y.; Wei, M.; Evans, D.G.; Duan, X. Hierarchical Nanowire Arrays Based on ZnO Core-Layered Double Hydroxide Shell for Largely Enhanced Photoelectrochemical Water Splitting. *Adv. Funct. Mater.* **2014**, *24*, 580–586. [[CrossRef](#)]
24. Trang, N.T.H.; Ngoc, H.V.; Lingappan, N.; Kang, D.J. A comparative study of supercapacitive performances of nickel cobalt layered double hydroxides coated on ZnO nanostructured arrays on textile fibre as electrodes for wearable energy storage devices. *Nanoscale* **2014**, *6*, 2434–2439. [[CrossRef](#)] [[PubMed](#)]
25. Guo, Q.S.; Zhang, Q.H.; Wang, H.Z.; Liu, Z.F.; Zhao, Z. Core-shell structured ZnO@Cu-Zn-Al layered double hydroxides with enhanced photocatalytic efficiency for CO<sub>2</sub> reduction. *Catal. Commun.* **2016**, *77*, 118–122. [[CrossRef](#)]
26. Hadnadjev-Kostic, M.; Vulic, T.; Marinkovic-Neducin, R. Solar light induced rhodamine B degradation assisted by TiO<sub>2</sub>-Zn-Al LDH based photocatalysts. *Adv. Powder Technol.* **2014**, *25*, 1624–1633. [[CrossRef](#)]
27. Dou, Y.B.; Zhang, S.T.; Pan, T.; Xu, S.M.; Zhou, A.W.; Pu, M.; Yan, H.; Han, J.B.; Wei, M.; Evans, D.G.; et al. TiO<sub>2</sub>@ Layered Double Hydroxide Core-Shell Nanospheres with Largely Enhanced Photocatalytic Activity Toward O<sub>2</sub> Generation. *Adv. Funct. Mater.* **2015**, *25*, 2243–2249. [[CrossRef](#)]
28. Seftel, E.M.; Niarchos, M.; Mitropoulos, C.; Mertens, M.; Vansant, E.F.; Cool, P. Photocatalytic removal of phenol and methylene-blue in aqueous media using TiO<sub>2</sub>@LDH clay nanocomposites. *Catal. Today* **2015**, *252*, 120–127. [[CrossRef](#)]
29. Yan, R.-Q.; Liu, G.-H.; Wang, Q.-F.; Liu, W.; Song, C.-L. Fast Photodegradation of Malachite Green using Nano-ZnO on Ceramic MgAl Carbonate Layered Double Hydroxides Support. *Chin. J. Chem. Phys.* **2016**, *29*, 241–244. [[CrossRef](#)]
30. Hosseini, S.A.; Akbari, M. ZnO/Mg-Al Layered Double Hydroxides as a Photocatalytic Bleaching of Methylene Orange - A Black Box Modeling by Artificial Neural Network. *Bull. Chem. React. Eng. Catal.* **2016**, *11*. [[CrossRef](#)]
31. Chen, D.; Li, Y.; Zhang, J.; Zhou, J.Z.; Guo, Y.; Liu, H. Magnetic Fe<sub>3</sub>O<sub>4</sub>/ZnCr-layered double hydroxide composite with enhanced adsorption and photocatalytic activity. *Chem. Eng. J.* **2012**, *185*, 120–126. [[CrossRef](#)]
32. Lester, E.; Blood, P.; Denyer, J.; Giddings, D.; Azzopardi, B.; Poliakoff, M. Reaction engineering: The supercritical water hydrothermal synthesis of nano-particles. *J. Supercrit. Fluids* **2006**, *37*, 209–214. [[CrossRef](#)]
33. Cheng, B.; Samulski, E.T. Hydrothermal synthesis of one-dimensional ZnO nanostructures with different aspect ratios. *Chem. Commun.* **2004**, 986–987. [[CrossRef](#)] [[PubMed](#)]
34. Zhao, Y.; Li, F.; Zhang, R.; Evans, D.G.; Duan, X. Preparation of layered double-hydroxide nanomaterials with a uniform crystallite size using a new method involving separate nucleation and aging steps. *Chem. Mater.* **2002**, *14*, 4286–4291. [[CrossRef](#)]
35. Wang, Q.; Tang, S.; Lester, E.; O'Hare, D. Synthesis of ultrafine layered double hydroxide (LDHs) nanoplates using a continuous-flow hydrothermal reactor. *Nanoscale* **2013**, *5*, 114–117. [[CrossRef](#)] [[PubMed](#)]
36. Miyata, S.; Okada, A. SYNTHESIS OF HYDROTALCITE-LIKE COMPOUNDS AND THEIR PHYSICO-CHEMICAL PROPERTIES - SYSTEMS MG<sup>2+</sup>-AL<sup>3+</sup>-SO<sub>4</sub><sup>2-</sup> AND MG<sup>2+</sup>-AL<sup>3+</sup>-CRO<sub>4</sub><sup>2-</sup>. *Clays Clay Miner.* **1977**, *25*, 14–18. [[CrossRef](#)]
37. Lee, K.M.; Lai, C.W.; Ngai, K.S.; Juan, J.C. Recent developments of zinc oxide based photocatalyst in water treatment technology: A review. *Water Res.* **2016**, *88*, 428–448. [[CrossRef](#)] [[PubMed](#)]
38. Marsalek, R. Particle Size and Zeta Potential of ZnO. *APCBEE Proc.* **2014**, *9*, 13–17. [[CrossRef](#)]
39. Thommes, M.; Kaneko, K.; Neimark, A.V.; Olivier, J.P.; Rodriguez-Reinoso, F.; Rouquerol, J.; Sing, K.S.W. Physisorption of gases, with special reference to the evaluation of surface area and pore size distribution (IUPAC Technical Report). *Pure Appl. Chem.* **2015**, *87*, 1051–1069. [[CrossRef](#)]
40. Clark, I. *Continuous Synthesis and Characterisation of Layered Double Hydroxide Nanomaterials for their Application for Dye Wastewater Remediation*; University of Nottingham: Nottingham, UK, 2018.
41. Rives, V. *Layered Double Hydroxides: Present and Future*; Nova Science Publishers: Huntington, NY, USA, 2001; pp. 1–439.
42. Islam, M.; Patel, R. Synthesis and physicochemical characterization of Zn/Al chloride layered double hydroxide and evaluation of its nitrate removal efficiency. *Desalination* **2010**, *256*, 120–128. [[CrossRef](#)]
43. Ogawa, M.; Kaiho, H. Homogeneous precipitation of uniform hydrotalcite particles. *Langmuir* **2002**, *18*, 4240–4242. [[CrossRef](#)]

44. Miyata, S. Physico-chemical Properties of Synthetic Hydrotalcites in Relation to Composition. *Clays Clay Miner.* **1980**, *28*, 50–56. [[CrossRef](#)]
45. Parker, L.M.; Milestone, N.B.; Newman, R.H. The use of hydrotalcite as an anion absorbent. *Ind. Eng. Chem. Res.* **1995**, *34*, 1196–1202. [[CrossRef](#)]

**Publisher’s Note:** MDPI stays neutral with regard to jurisdictional claims in published maps and institutional affiliations.



© 2020 by the authors. Licensee MDPI, Basel, Switzerland. This article is an open access article distributed under the terms and conditions of the Creative Commons Attribution (CC BY) license (<http://creativecommons.org/licenses/by/4.0/>).